

SUPPORTING INFORMATION

A Thermochemical Study of Iron Aluminate-Based Materials: A Preferred Class for Isothermal Water Splitting

Kent J. Warren^{a,*}, Justin T. Tran^a, and Alan W. Weimer^{a,*}

^a Department of Chemical and Biological Engineering, University of Colorado, Boulder, Colorado 80309-0596, United States

* Corresponding authors: Email Addresses: kent.warren@colorado.edu,
alan.weimer@colorado.edu

S.1. Supporting Figures and Tables

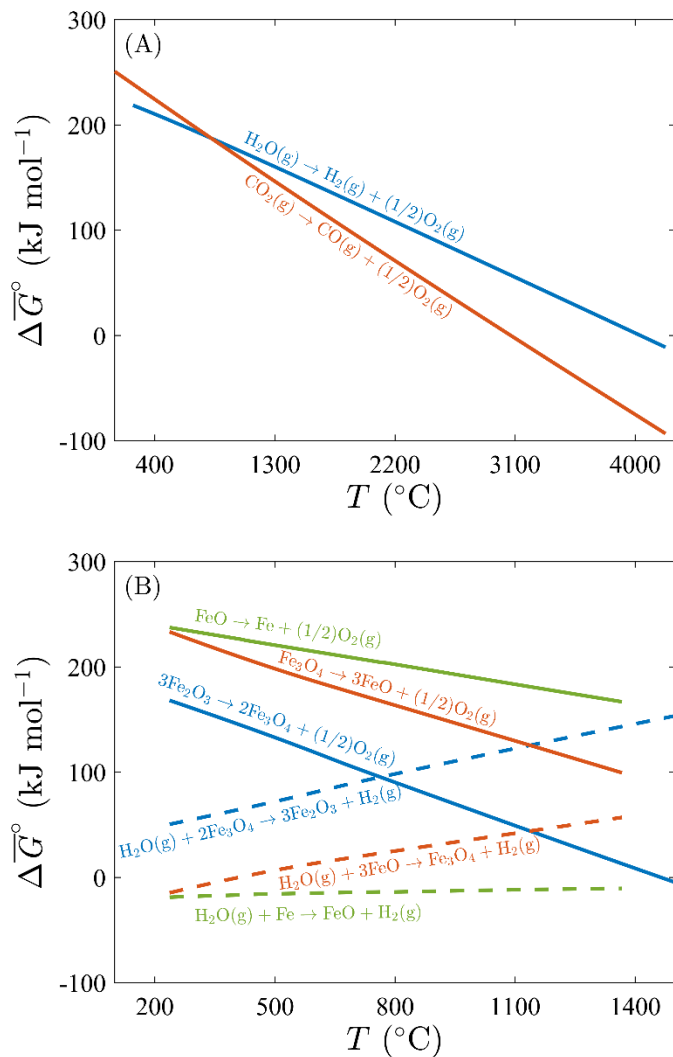


Figure S1. Standard molar Gibbs energy change, plotted as a function of temperature at 1 bar, for (A) the thermolysis of H_2O and CO_2 and (B) three thermochemical water-splitting cycles based on iron oxide redox pairs, where solid and dashed lines correspond to reduction and oxidation reactions, respectively. Early work considered using the $\text{Fe}_3\text{O}_4/\text{FeO}$ redox system,¹ as, among other reasons, the thermal reduction of Fe_3O_4 is less endothermic than that of FeO , and water splitting over Fe_3O_4 is not thermodynamically feasible. For these calculations, the necessary thermodynamic data was extracted from the NIST-JANAF Thermochemical Tables² or the NIST Chemistry WebBook.³

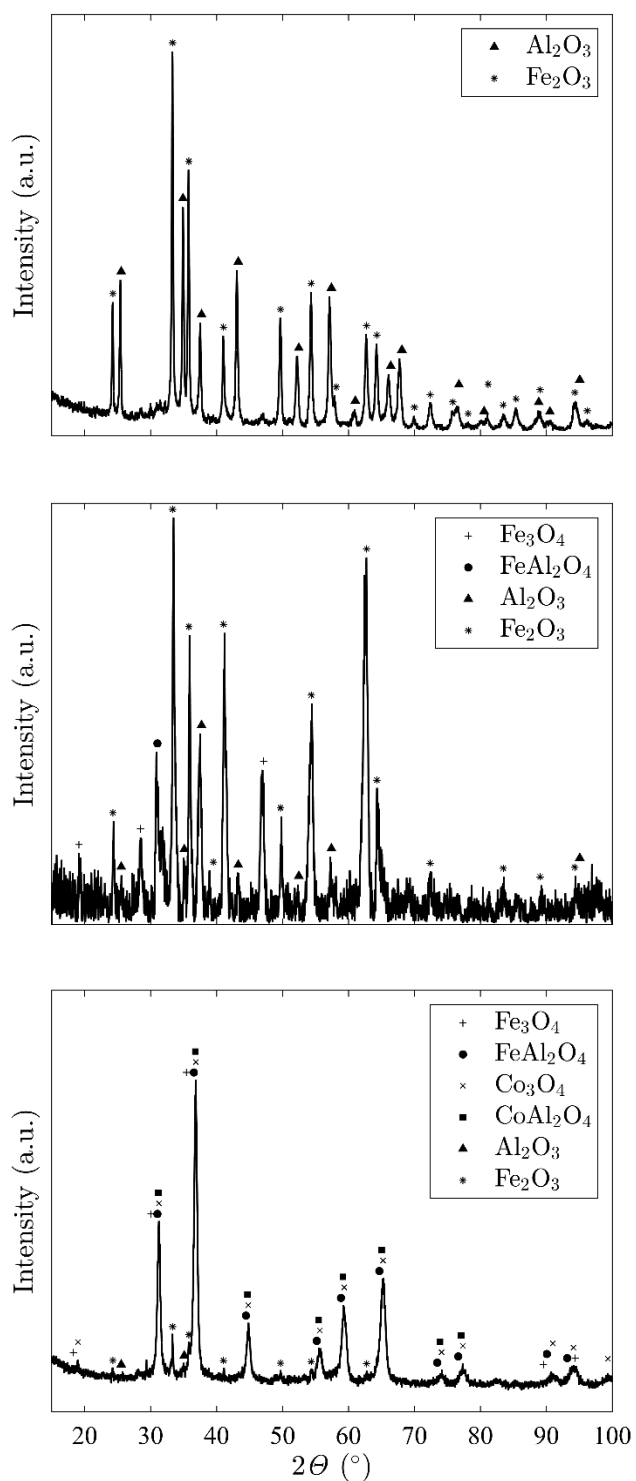


Figure S2. Powder X-ray diffraction patterns of the iron aluminate-based materials following calcination in air at 850 °C for 24 hours. The top, middle, and bottom panels correspond to Fe₃₃Al₆₇, Fe₄₇Al₅₃, and Co₁₃Fe₂₀Al₆₇, respectively.

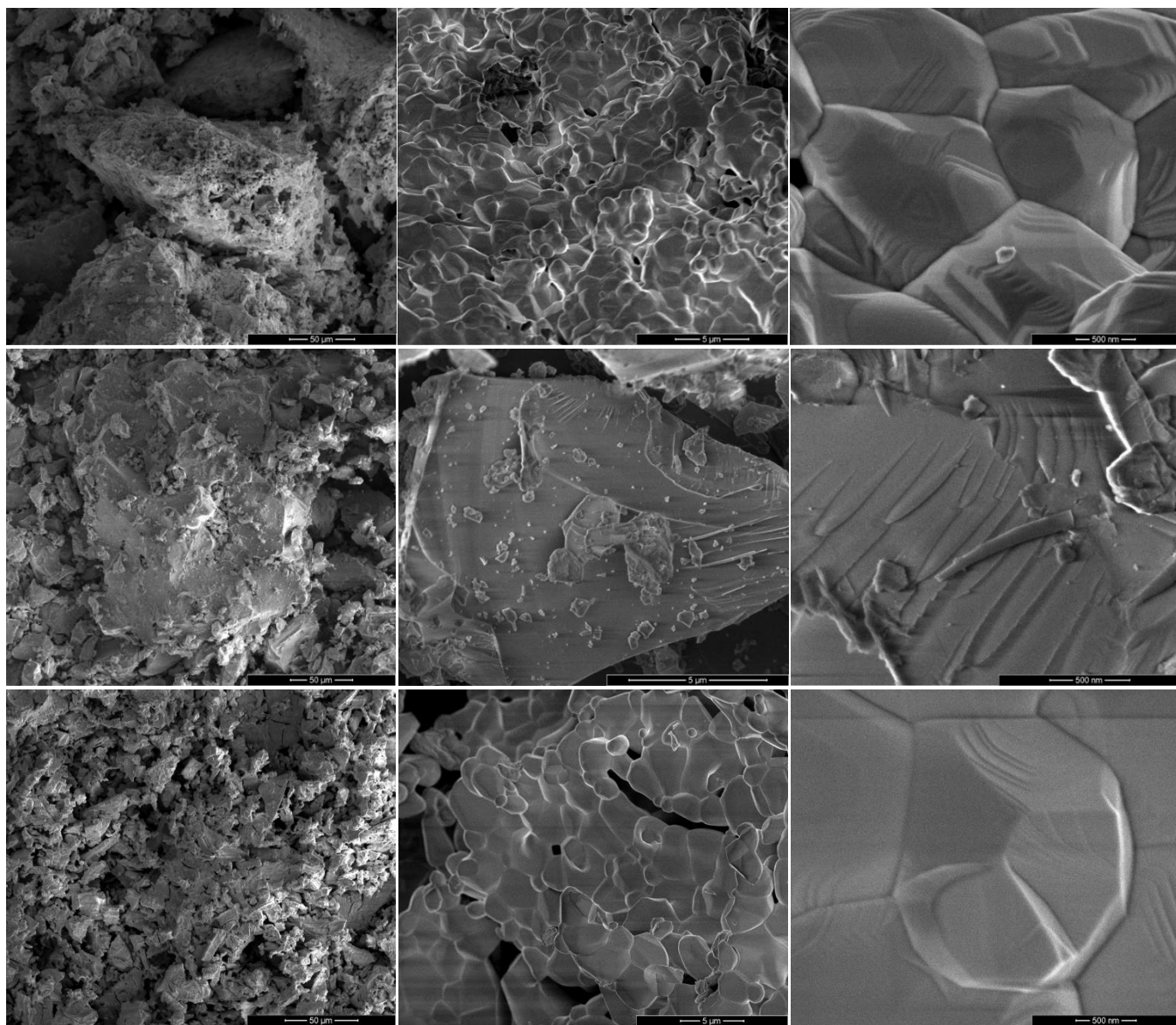


Figure S3. Scanning electron micrographs of the as-synthesized iron aluminate-based materials, where the top, middle, and bottom rows correspond to $\text{Fe}_{33}\text{Al}_{67}$, $\text{Fe}_{47}\text{Al}_{53}$, and $\text{Co}_{13}\text{Fe}_{20}\text{Al}_{67}$, respectively. From left to right, each row is arranged in order of increasing magnification.

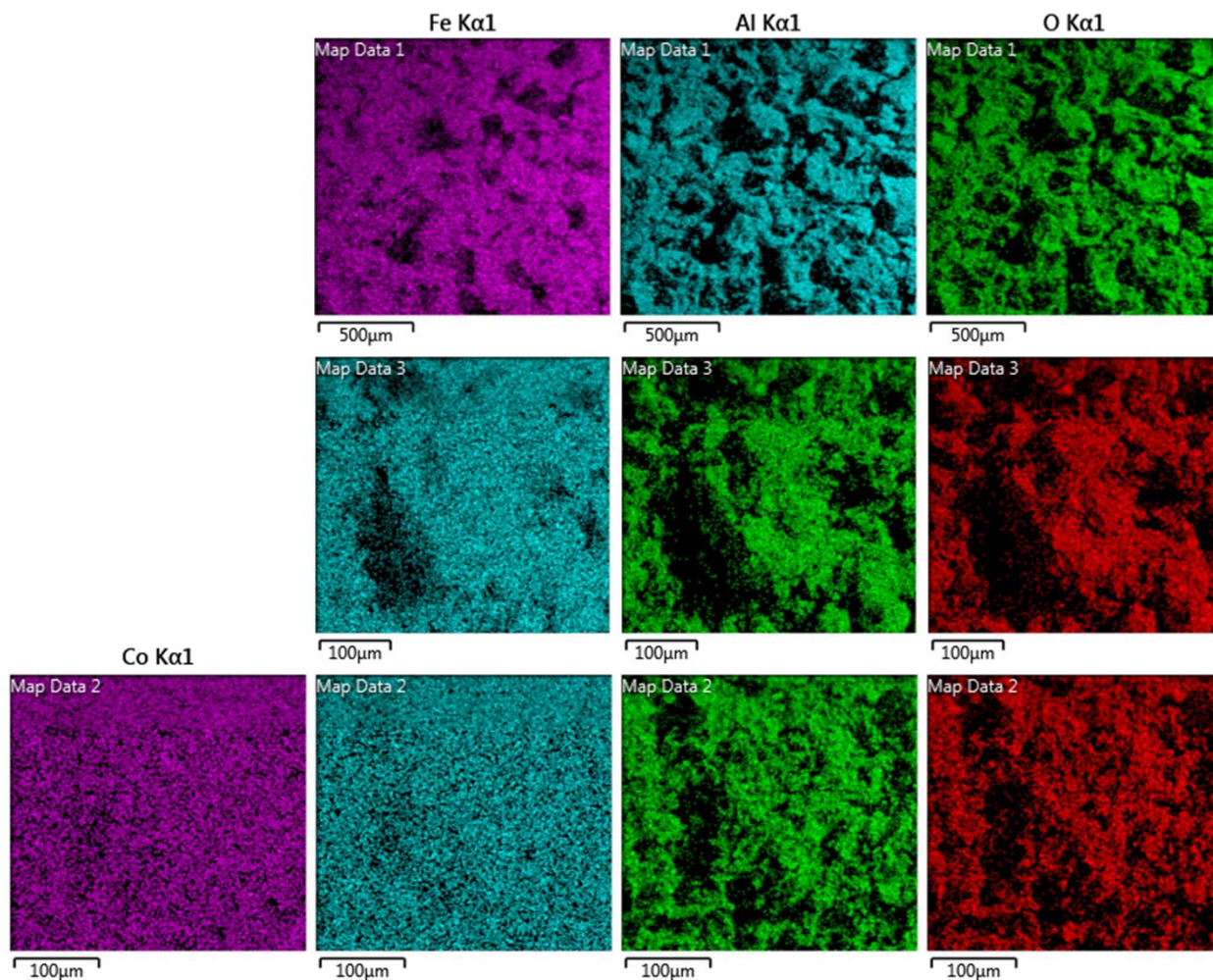


Figure S4. Energy dispersive X-ray spectroscopy images of the as-synthesized iron aluminate-based materials, where the top, middle, and bottom rows correspond to $\text{Fe}_{33}\text{Al}_{67}$, $\text{Fe}_{47}\text{Al}_{53}$, and $\text{Co}_{13}\text{Fe}_{20}\text{Al}_{67}$, respectively. From left to right, each column refers to a detected element, i.e., Co, Fe, Al, and O.

Table S1. Structural refinement parameters for Fe33Al67 and Fe47Al53 following synthesis and the experimental campaign.

Sample	Phase	χ^2	Space Group	a [Å]	b [Å]	c [Å]	α [°]	β [°]	γ [°]	Volume [Å ³]
Fe33Al67	As-Synthesized	7.98								
	FeAl ₂ O ₄		<i>Fd-3m</i>	8.16079	8.16079	8.16079	90	90	90	543.497
	Fe ₃ O ₄		<i>Fd-3m</i>	8.16085	8.16085	8.16085	90	90	90	543.508
	Post-Cycled	1.56								
	FeAl ₂ O ₄		<i>Fd-3m</i>	8.36137	8.36137	8.36137	90	90	90	584.564
	Fe ₃ O ₄		<i>Fd-3m</i>	8.33257	8.33257	8.33257	90	90	90	578.544
	Fe ₂ O ₃		<i>R-3c</i>	5.00042	5.00042	13.6271	90	90	120	295.085
Al ₂ O ₃		<i>R-3c</i>	4.77961	4.77961	13.03648	90	90	120	257.915	
Fe47Al53	As-Synthesized	7.53								
	FeAl ₂ O ₄		<i>Fd-3m</i>	8.2124(3)	8.2124(3)	8.2124(3)	90	90	90	553.88(4)
	Fe ₃ O ₄		<i>Fd-3m</i>	8.2200(5)	8.2200(5)	8.2200(5)	90	90	90	555.42(6)
	Post-Cycled	5.38								
	FeAl ₂ O ₄		<i>Fd-3m</i>	8.3539(6)	8.3539(6)	8.3539(6)	90	90	90	583.01(7)
	Fe ₃ O ₄		<i>Fd-3m</i>	8.348(2)	8.348(2)	8.348(2)	90	90	90	581.8(2)
	Fe ₂ O ₃		<i>R-3c</i>	4.9993(2)	4.9993(2)	13.615(1)	90	90	120	294.71(3)
Al ₂ O ₃		<i>R-3c</i>	4.7914(4)	4.7914(4)	13.065(2)	90	90	120	259.75(6)	

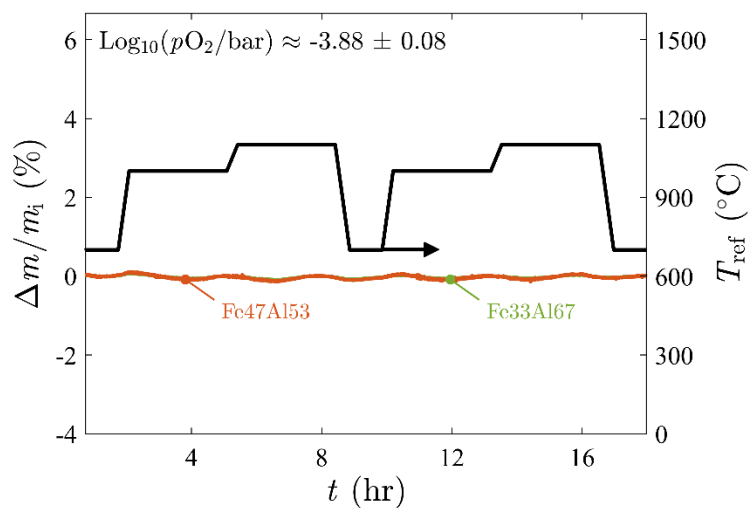


Figure S5. Representative thermogravimetric experiment using an altered procedure, where isotherms were elongated to ensure equilibrium was attained at each condition. Percent relative change in mass from the fully oxidized state (colored lines) and reference temperature (black line) as a function of time at a particular oxygen partial pressure: $p_{O_2} \approx 1.32 \times 10^{-4} \pm 2.53 \times 10^{-5}$ bar.

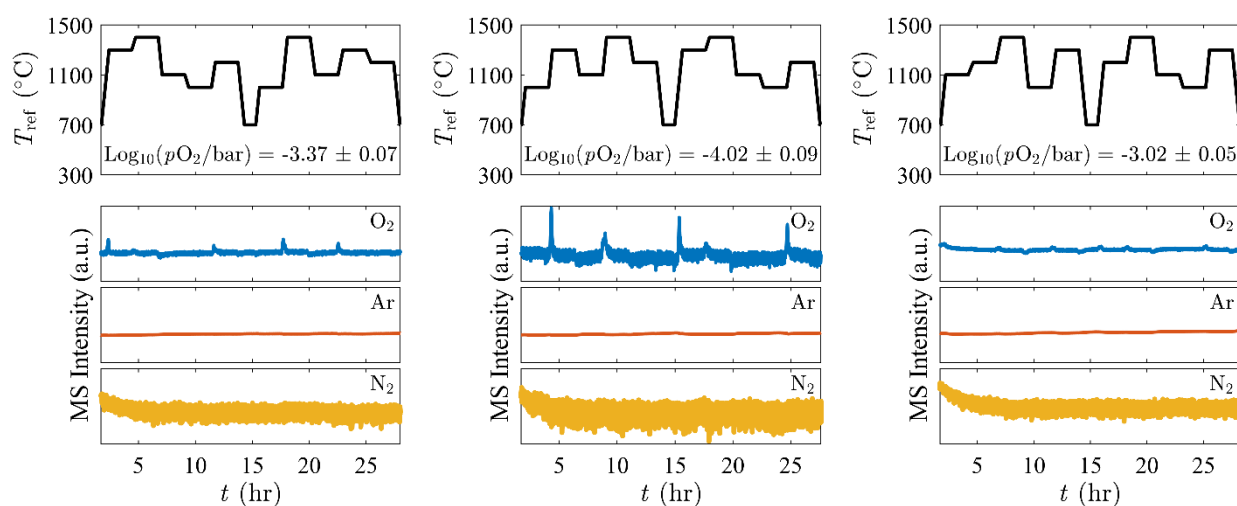
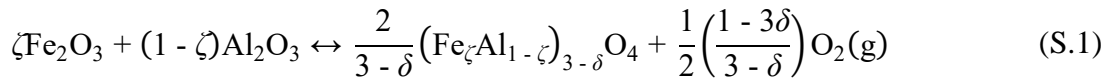


Figure S6. Residual gas analysis of representative experiments, where samples are subjected to changes in temperature at a constant oxygen partial pressure. The operating conditions and mass spectrometer measurements are shown in the top and bottom panels, respectively, while, the left, middle, and right figures correspond to experiments with Fe₃₃Al₆₇, Fe₄₇Al₅₃, and Co₁₃Fe₂₀Al₆₇ pellets. Importantly, qualitative changes in the O₂ signal (from evolution or consumption) are observed without any concomitant response in the signals that correspond to delivered Ar or baseline N₂ (i.e., noise), thus implying that ambient air does not influence the reported thermogravimetric measurements. Note that, in the bottom panels, the difference between the maximum and minimum values of each ordinate axis is equivalent.

S.2. Quantifying Cation Nonstoichiometry, δ

Generally, for oxides that accommodate oxygen vacancies (e.g., $\text{CeO}_{2-\delta}$), the fully oxidized and stoichiometric (i.e., $\delta = 0$) states are synonymous, and as a result, these terms are often used interchangeably in literature. However, for iron-containing oxides, such as those evaluated in this study and others^{4,5}, the presence of cation vacancies in certain phases separates the fully oxidized state from where all vacancies are filled. For example, according to Figures 2 and 4 of the manuscript, the fully oxidized state of iron aluminates is composed of hematite (Fe_2O_3) and corundum (Al_2O_3), whereas significant deviations from stoichiometry are only observed after the transition to a spinel solid solution occurs. The chemical equation of this phase transition may be represented as follows:



Note that the fully oxidized state is defined as the equilibrium composition of the iron aluminate under ambient conditions (i.e., room temperature and atmospheric pressure), the notation for spinel solid solution is adopted from Nakamura et al.,⁶ and ζ refers to the cation composition such that ζ equals 0.33 and 0.47 for Fe33Al67 and Fe47Al53, respectively.

A close inspection of Equation S.1 reveals that, unlike oxygen-vacancy-mediated mechanisms, the extent of reduction (i.e., oxygen removal) increases with decreasing degree of nonstoichiometry (δ), thus implying that the stoichiometric state of the spinel solid solution exists under conditions more reducing than that required for initiating the phase transition. This distinction between states (i.e., fully oxidized vs. stoichiometric) introduces a challenge in quantifying δ , as its magnitude is referenced to when the spinel solid solution is stoichiometric, which – in this case – occurs at an unknown T and $p\text{O}_2$. As previously demonstrated for magnetite ($\text{Fe}_{3-\delta}\text{O}_4$), an extensive thermogravimetric analysis can be used to physically locate the conditions where $\delta = 0$;⁷ however, in this study, uncertainty related to the required $p\text{O}_2$ (and the potential inability to experimentally control such $p\text{O}_2$) motivated the following alternative approach, which leverages reaction stoichiometry to quantify δ .

According to the stoichiometry of Equation S.1, the mass (m) of an iron aluminate at the fully oxidized and stoichiometric (i.e., $\delta = 0$) states can be related – as shown in Equation S.2 – by quantifying the loss in mass that accompanies oxygen removal.

$$m_{\text{st}} = m_i \left(1 - \frac{M_{\text{O}}}{3M_i}\right) \quad (\text{S.2})$$

Here, the subscript st refers to stoichiometric and the subscript i refers to initial, which, in the context of the experimental procedure presented in Section 2.1.2., corresponds to the sample in its fully oxidized state. In addition, the molar masses of oxygen and the hematite–corundum solid solution are denoted by M_{O} and M_i , respectively. The latter, as shown in Equation S.3, is defined as the sum of the molar masses of each component, scaled by the cation composition (i.e., mole fraction).

$$M_i = \zeta M_{\text{Fe}_2\text{O}_3} + (1 - \zeta) M_{\text{Al}_2\text{O}_3} \quad (\text{S.3})$$

Therefore, with knowledge of the initial mass (which is measured before each experiment), the concomitant stoichiometric mass can be calculated even if the conditions (i.e., T and $p\text{O}_2$) where it occurs are unknown. Deviations from stoichiometry (i.e., δ) may then be determined using the conventional method of measuring the equilibrated change in mass relative to a reference state of known composition.⁸ For iron aluminates in the spinel solid solution phase, a (positive) change in mass from the (reference) stoichiometric state represents the number of moles (n) of monatomic oxygen consumed from the surrounding atmosphere, which – as shown in Equation S.4 – is proportional to the number of moles of cation vacancies (n_v) formed.

$$n_v = \frac{m_{\text{eq}} - m_{\text{st}}}{1} \cdot \frac{\cancel{\text{g}}}{1} \cdot \frac{1}{M_{\text{O}}} \cdot \frac{\cancel{\text{mol}}_{\text{O}}}{\cancel{\text{g}}} \cdot \frac{3 \cancel{\text{mol}}_{\text{cations}}}{4 \cancel{\text{mol}}_{\text{O}}} \cdot \frac{1 \text{ mol}_v}{1 \cancel{\text{mol}}_{\text{cations}}} \quad (\text{S.4})$$

Similarly, the number of moles of the spinel solid solution in its stoichiometric state (n_{st}) is given by Equation S.5

$$n_{\text{st}} = \frac{m_{\text{st}}}{1} \cdot \frac{\cancel{\text{g}}}{1} \cdot \frac{1}{M_{\text{st}}} \cdot \frac{\text{mol}_{\text{st}}}{\cancel{\text{g}}} \quad (\text{S.5})$$

where M_{st} , as shown in Equation S.6, refers to the molar mass at the corresponding composition.

$$M_{\text{st}} = 3\zeta M_{\text{Fe}} + 3(1 - \zeta) M_{\text{Al}} + 4M_{\text{O}} \quad (\text{S.6})$$

The molar ratio of cation vacancies to the spinel solid solution in its stoichiometric state (i.e., n_v/n_{st}) yields the expression for δ defined in Equation 3 of the manuscript. To help visualize the relevant parameters used to quantify δ , a schematic – in the form of a thermogravimetric measurement – is presented in Figure S7.

While this approach can be analogously applied to quantify δ for cobalt iron aluminates, the presence of Co_3O_4 and CoAl_2O_4 in the fully oxidized state (see Figures 2 and S2) renders computation of M_i impossible without additional information regarding the exact proportion of each cobalt-containing component.

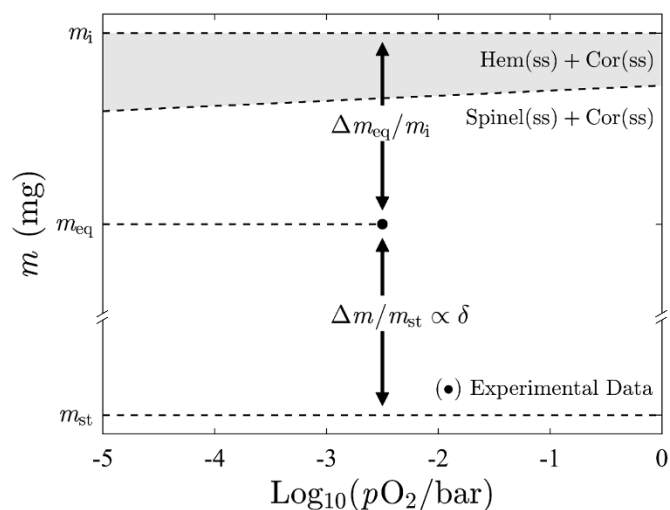


Figure S7. Schematic illustration of the relevant parameters for quantifying cation nonstoichiometry (δ) in, for example, iron-aluminates. Relevant parameters include m_i , m_{eq} , and m_{st} , which correspond to the initial (fully oxidized) mass, equilibrated mass at a particular T_{ref} and $p\text{O}_2$, and stoichiometric mass, respectively. The shaded region represents the phase where a solid solution of hematite and corundum is observed, and the iron-aluminate is fully oxidized. Unlike redox materials that accommodate oxygen vacancies (e.g., $\text{CeO}_{2-\delta}$), the fully oxidized and stoichiometric states of the spinel solid solutions considered herein are – for a given T – established at different ranges of $p\text{O}_2$; as a result, the masses at each state are unique.

S.3. Uncertainty Analysis

The propagation of measurement uncertainty to the reported results (e.g., pO_2 , $\Delta m_{eq}/m_i$, and δ) was determined at a 95% confidence level via the root-sum-squares method.⁹ Relevant elemental errors are presented in Table S2.

Table S2. Elemental errors of equipment used for experimentation.

Supplier	Component	Resolution	Uncertainty	Repeatability
Bronkhorst	EL-FLOW Select F-201CV	0.1 mL _N min ⁻¹	± 0.5% of Rd ± 0.1% of FS	< ± 0.2% of Rd
Vögtlin Instruments	Q-Flow 140	10 mL _N min ⁻¹	± 2% of FS	
Mesa Labs	FlexCal M		± 0.5% of Rd	
Airgas	Certified Standard Gas Mixture		± 2% of M	
US National Weather Service	KBDU Barometer		< ± 1 mbar	
NETZSCH	STA 449 F1 Jupiter	0.025 µg		
	Type S Thermocouple		± 0.25% of Rd	
CAI	700 Series NDIR (FS _{CO} = 5 vol. %)	± 0.1% of FS	± 1% of FS	< ± 1% of FS
AMI	Model 2001 RS (FS _{O₂} = 500 ppm)	± 1% of Rd	± 0.5% of FS	± 1% of FS

Abbreviations: Rd, reading; FS, full scale; M, measurand.

S.4. Chemical Defect Equilibria of Ceria and Doped Lanthanum Manganites

Our methods of obtaining thermodynamic state quantities (i.e., $\Delta\bar{H}^\circ$ and $\Delta\bar{S}^\circ$) of iron aluminate spinel solid solutions are analogous to those used in studies concerned with assessing the water-splitting capability of materials that accommodate oxygen vacancies, namely ceria-based oxides¹⁰ and doped lanthanum manganites.^{11, 12} Regardless of the mechanism by which reduction and oxidation occur, this approach to determining material properties remains valid as long as (1) the proposed defect reactions are appropriate and (2) the equilibrium constant (K) equations adequately describe the experimental data (e.g., equilibrium δ vs. $p\text{O}_2$ isotherms). Generally, the fitting procedure involves using δ measurements to evaluate algebraically simplified expressions for K at a constant temperature before extracting $\Delta\bar{H}^\circ$ and $\Delta\bar{S}^\circ$ (for each defect reaction considered) from the best linear fit to the van't Hoff equation: $\ln K = -\Delta\bar{H}^\circ/RT + \Delta\bar{S}^\circ/R$. In this study, however, rather than adopt temperature-dependent fitting methods, $\Delta\bar{H}^\circ$ and $\Delta\bar{S}^\circ$ were obtained as discussed in Sections 2.2.2 and 3.1 of the manuscript, by minimizing the error between the measurements (δ) and model predictions (δ_{model}) for all conditions examined (i.e., T and $p\text{O}_2$).

To validate our approach for solving this global optimization problem, existing defect models for the formation of oxygen vacancies in $\text{CeO}_{2-\delta}$ ¹⁰ and $\text{La}_{0.6}\text{Sr}_{0.4}\text{Mn}_{0.6}\text{Al}_{0.4}\text{O}_{3-\delta}$ ¹², summarized in Table S3, were reproduced and evaluated using both aforementioned methods of extracting $\Delta\bar{H}^\circ$ and $\Delta\bar{S}^\circ$. Our model predictions, superimposed on the digitized experimental data, and the resulting equilibrium constant expressions, as compared to previous work, are presented in Figure S8. In general, for each defect reaction, our expressions for K agree well with those derived via the alternative, temperature-dependent fitting method; however, circumventing the need to use δ measurements as a model input allows for materials with more complex defect chemistries, such as iron aluminates, to be effectively modeled without sacrificing important mechanistic information.

Table S3. Summation of defect models previously employed to extract thermodynamic state properties of oxygen vacancy formation in $\text{CeO}_{2-\delta}^{10}$ and $\text{La}_{0.6}\text{Sr}_{0.4}\text{Mn}_{0.6}\text{Al}_{0.4}\text{O}_{3-\delta}$.¹²

Redox Material	Defect Mechanisms	Conservation Equations
Ceria	Reduction of tetravalent Ce, K_1 : $2\text{Ce}_{\text{Ce}}^{\times} + \text{O}_{\text{O}}^{\times} \leftrightarrow 2\text{Ce}'_{\text{Ce}} + \text{V}_{\text{O}}^{\bullet\bullet} + 1/2\text{O}_2(\text{g})$	O-site balance: $[\text{O}_{\text{O}}^{\times}] + [\text{V}_{\text{O}}^{\bullet\bullet}] + [(\text{Ce}'_{\text{Ce}}\text{V}_{\text{O}}^{\bullet\bullet}\text{Ce}'_{\text{Ce}})^{\times}] = 2$
	Formation of defect associations, K_2 : $2\text{Ce}'_{\text{Ce}} + \text{V}_{\text{O}}^{\bullet\bullet} \leftrightarrow (\text{Ce}'_{\text{Ce}}\text{V}_{\text{O}}^{\bullet\bullet}\text{Ce}'_{\text{Ce}})^{\times}$	Ce-site balance: $[\text{Ce}_{\text{Ce}}^{\times}] + [\text{Ce}'_{\text{Ce}}] + 2[(\text{Ce}'_{\text{Ce}}\text{V}_{\text{O}}^{\bullet\bullet}\text{Ce}'_{\text{Ce}})^{\times}] = 1$ Electroneutrality: $2[\text{V}_{\text{O}}^{\bullet\bullet}] = [\text{Ce}'_{\text{Ce}}]$ Oxygen nonstoichiometry: $\delta_{\text{model}} = [\text{V}_{\text{O}}^{\bullet\bullet}] + [(\text{Ce}'_{\text{Ce}}\text{V}_{\text{O}}^{\bullet\bullet}\text{Ce}'_{\text{Ce}})^{\times}]$
LSMA6464	Reduction of tetravalent Mn, K_1 : $2\text{Mn}_{\text{Mn}}^{\bullet} + \text{O}_{\text{O}}^{\times} \leftrightarrow 2\text{Mn}_{\text{Mn}}^{\times} + \text{V}_{\text{O}}^{\bullet\bullet} + 1/2\text{O}_2(\text{g})$	O-site balance: $[\text{O}_{\text{O}}^{\times}] + [\text{V}_{\text{O}}^{\bullet\bullet}] = 3$
	Disproportionation of trivalent Mn, K_2 : $\text{Mn}_{\text{Mn}}^{\bullet} + \text{O}_{\text{O}}^{\times} \leftrightarrow \text{Mn}'_{\text{Mn}} + \text{V}_{\text{O}}^{\bullet\bullet} + 1/2\text{O}_2(\text{g})$	Mn-site balance: $[\text{Mn}_{\text{Mn}}^{\bullet}] + [\text{Mn}_{\text{Mn}}^{\times}] + [\text{Mn}'_{\text{Mn}}] = 0.6$ Electroneutrality: $[\text{Mn}_{\text{Mn}}^{\bullet}] + 2[\text{V}_{\text{O}}^{\bullet\bullet}] = [\text{Mn}'_{\text{Mn}}] + 0.4$ Oxygen nonstoichiometry: $\delta_{\text{model}} = [\text{V}_{\text{O}}^{\bullet\bullet}]$

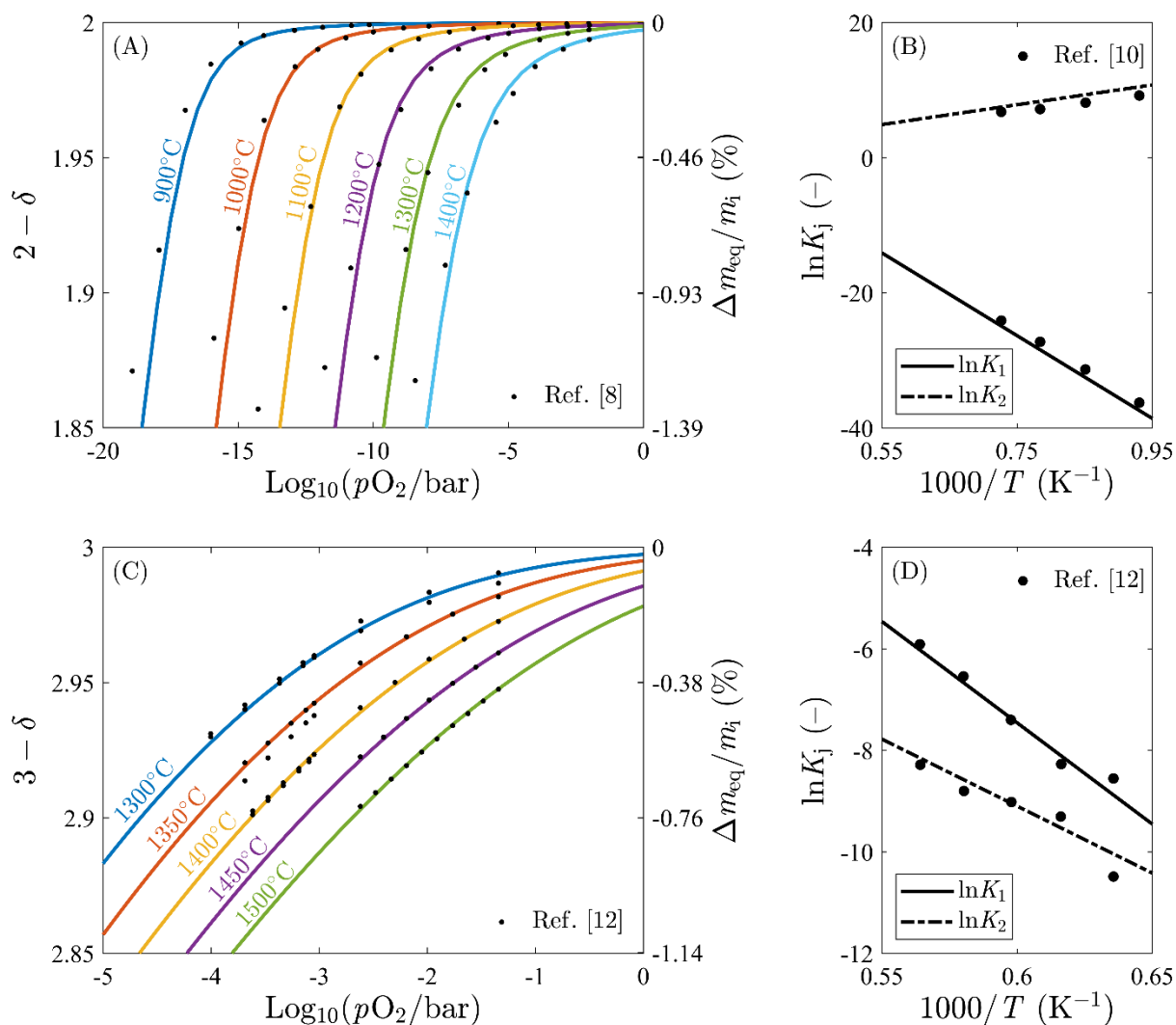


Figure S8. Select equilibrium oxygen nonstoichiometry (δ) measurements (symbols) of (A) ceria⁸ and (C) LSMA6464¹² as a function of T and $p\text{O}_2$; the corresponding relative mass change between the fully oxidized (i.e., stoichiometric) and equilibrium states is reported on the right ordinate. Colored lines indicate our defect model predictions (δ_{model}). Resulting equilibrium constants versus inverse temperature (solid and dashed lines) for (B) ceria and (D) LSMA6464 as compared to previous work (symbols)^{10,12}, which adopted temperature-dependent fitting methods.

References for Supporting Information

1. T. Nakamura, *Solar energy*, 1977, **19**, 467-475.
2. M. W. Chase, Jr, *J. Phys. Chem. Ref. Data, Monogr.*, 1998, **9**.
3. P. J. Linstrom and W. G. Mallard, *Journal of Chemical & Engineering Data*, 2001, **46**, 1059-1063.
4. J. Töpfer, S. Aggarwal and R. Dieckmann, *Solid State Ionics*, 1995, **81**, 251-266.
5. K. N. Krafft and M. Martin, *The Korean Journal of Ceramics*, 1998, **4**, 156-161.
6. A. Nakamura, S. Yamauchi, K. Fueki and T. Mukaibo, *Bulletin of the Chemical Society of Japan*, 1979, **52**, 1019-1026.
7. R. Dieckmann, *Berichte der Bunsengesellschaft für physikalische Chemie*, 1982, **86**, 112-118.
8. R. Panlener, R. Blumenthal and J. Garnier, *Journal of Physics and Chemistry of Solids*, 1975, **36**, 1213-1222.
9. R. S. Figliola and D. E. Beasley, *Theory and design for mechanical measurements*, John Wiley & Sons, 2014.
10. J. R. Scheffe and A. Steinfeld, *Energy & fuels*, 2012, **26**, 1928-1936.
11. T. Cooper, J. R. Scheffe, M. E. Galvez, R. Jacot, G. Patzke and A. Steinfeld, *Energy Technology*, 2015, **3**, 1130-1142.
12. M. Takacs, M. Hoes, M. Caduff, T. Cooper, J. Scheffe and A. Steinfeld, *Acta Materialia*, 2016, **103**, 700-710.